Nano Research
2019, 12(8): 1931–1936

ISSN 1998-0124 CN 11-5974/O4
https://doi.org/10.1007/s12274-019-2460-2

Research Article

Modulating the photoelectrons of g-C_3N_4 via coupling $MgTi_2O_5$ as appropriate platform for visible-light-driven photocatalytic solar energy conversion

Jiaxin Shen[1], Yanzhen Li[1], Haoying Zhao[1], Kai Pan[1], Xue Li[1] (✉), Yang Qu[1] (✉), Guofeng Wang[1] (✉), and Dingsheng Wang[2]

[1] *Key Laboratory of Functional Inorganic Material Chemistry, Ministry of Education, School of Chemistry and Materials Science, Heilongjiang University, Harbin 150080, China*
[2] *Department of Chemistry, Tsinghua University, Beijing 100084, China*

Received: 15 April 2019 / **Revised:** 27 May 2019 / **Accepted:** 5 June 2019

ABSTRACT

Graphitic carbon nitride (g-C_3N_4) has become an attractive visible-light-responsive photocatalyst because of its semiconductor polymer compositions and easy-modulated band structure. However, the bulk g-C_3N_4 photocatalyst has the low separation efficiency of photogenerated carriers and unsatisfied surface catalytic performance, which leads to poor photocatalytic performance. As for this, $MgTi_2O_5$ with high chemical stability, wide band gap and negative conduction band was used as a suitable platform for coupling with g-C_3N_4 to enhance charge separation and promoted the photoactivity. Different from common approaches, here, we propose an innovative method to construct g-C_3N_4/$MgTi_2O_5$ nanocomposites featuring "0 + 1 > 1" magnification effect to improve g-C_3N_4 photocatalytic performance under visible light irradiation. Additionally, compositing metal oxides of $MgTi_2O_5$ with g-C_3N_4 has proven to be a proper strategy to accelerate surface catalytic reactions in g-C_3N_4, and the photoinduced carriers were modulated to maintain thermodynamic equilibrium, which convincingly promotes the photocatalytic activity. The photocatalytic performance of the nanocomposites was measured by hydrogen production and CO_2 reduction under visible light. The developed g-C_3N_4/$MgTi_2O_5$ nanocomposites with a 5 wt.% $MgTi_2O_5$ exhibits the highest H_2 and CO yield under visible light and excellent stability compare to the other $MgTi_2O_5$ contents in composites. According to surface photo-voltage spectra, electrochemical CO_2 reduction, photoluminescence, etc. The superior performance can be related to an enhanced electron lifetime, the promoted charge transfer and the increased electronic separation property of g-C_3N_4. Our work provides an approach to overcome the defect of pure g-C_3N_4, which accesses to composite with the second component matched well.

KEYWORDS

g-C_3N_4/$MgTi_2O_5$, visible-light, photocatalytic hydrogen production, CO_2 reduction

1 Introduction

Environmental sustainability and energy consumption are two main issues that the modern society faces. And solar energy attracts closer attention due to its cleanness and huge abundance. Since Fujishima and Honda reported photoelectrochemical water splitting in 1972 [1], photocatalysis has been regarded as one of the most promising way for converting solar light into hydrogen (H_2) energy. Since then, the photocatalytic degradation and the reduction of CO_2 to hydrocarbon compounds also became research hotspots [2, 3]. With the combustion of fossil fuels, the house-green effect and environmental pollution attract increasing attention. Both photocatalytic water splitting of producing H_2 employing semiconductor and photocatalytic reduction of CO_2 to hydrocarbon compounds are promising ways to convert solar energy to storable chemical fuel [4–9]. Therefore, the high-efficient, cost-effective and eco-friendly photocatalysts should be developed to solve the energy issues.

For enhancing the solar energy conversion efficiency, it is an urgent task to explore the visible-light-responsive photocatalysts [10, 11]. Graphitic-C_3N_4 (g-C_3N_4) nanosheet was extremely broadly applicable, which was extensively investigated as bioimaging [12, 13], biosensor [14], photocatalyst [15, 16]. Note that the g-C_3N_4 as a promising photocatalyst has attracted a great deal attention owing to its variety advantages [17], such as easy-modulated band structure, nontoxicity, and high quantum yield. The g-C_3N_4 with a semiconductor band structure possesses a wide bandgap (~ 2.7 eV), and the valence band (VB) top and the conduction band (CB) bottom are located at about + 1.4 eV and −1.1 eV, respectively. The sufficiently negative conduction band can benefit for photocatalytic performance [18]. Integrating g-C_3N_4 with second component may be a promising way to overcome this shortcoming [19]. Since Wang et al. first report the works about the photocatalytic hydrogen production on g-C_3N_4 in 2009 [20], research endeavors begin to enhance the photocatalytic activities of photocatalysts, which has set off a wave of interest in the photocatalytic research field. However, g-C_3N_4 still bears the low charge separation efficiency and a short lifetime [21], if they are exposed to a certain light irradiation over the time, they will become deactivated catalysts due to their unsatisfied surface catalytic performance. Inside g-C_3N_4-based photocatalysts, the recombination can be greatly suppressed due to their effective separation of photogenerated electrons and holes. Thus, suppressing the recombination of photo-induced charge carriers is extremely meaningful. Coupling

Address correspondence to Guofeng Wang, wanggf_w@163.com; Yang Qu, quyang@hlju.edu.cn; Xue Li, 1542547101@qq.com

with semiconductors with matched bandgap to form heterojunction photocatalyst can drive the charge separation due to the electric potential difference. As a result, the photoelectrons and holes are separated on the two semiconductors respectively, which have effectively facilitated the separation of photogeneration charge carriers. However, in such photocatalytic system, the nanocomposites as an electron-acceptor are often with lower CB potential, resulting in the reduced thermodynamic energy. Thus, choosing appropriate semiconductor to couple with g-C_3N_4 is much more important. Generally speaking, TiO_2 with the CB bottom at –0.2 e V has been widely used to couple with g-C_3N_4 [22]. Although the visible-light photoactivity of g-C_3N_4 was improved, the very large potential difference of g-C_3N_4 (–1.1 e V) and TiO_2 makes the serious waste of the thermodynamic energy [23–25]. Wide bandgap ones with much negative CB are highly desired.

In our previous works, we have found that alkali titanates possess of very negative CB and exhibited excellent photoactivity for H_2 production [26–28]. Compared with TiO_2, the alkali titanates exhibited a more negative conduction band, which have efficiently minimized energy loss of electronic transition [29, 30]. Especially, the $MgTi_2O_5$ as an important part of alkali titanates has been exerted to a variety of applications [31–36]. Since it possesses a proper electronic structure, a superior stability, a more negative conduction band, which can match well with other components [37]. According to the previous reports, the CB and VB of $MgTi_2O_5$ are located at −0.41 and +2.99 eV, respectively [38]. Innovative design of heterogeneous structure of g-C_3N_4/$MgTi_2O_5$ nanocomposites that possessing suitable band structures could availably enhance pure g-C_3N_4 photocatalytic performance, extend the electron lifetime, minimize energy loss, and suppress the recombination of electron- hole. Herein, we take $MgTi_2O_5$ as a reasonable platform to improve photocatalytic ability and to overcome the shortcomings of g-C_3N_4 by modulating photoelectrons in the heterojunction materials.

According to the above-discussed, reasonable mechanism for improved photocatalytic performance of H_2 production and CO_2 reduction has been indicated in Fig. 1. It shows the photoinduced electron transfer reaction of the g-C_3N_4/$MgTi_2O_5$ photocatalyst under visible light. $MgTi_2O_5$ may not be able to be excited by visible irradiation because of the unsuitable band gap, and g-C_3N_4 in the g-C_3N_4/ $MgTi_2O_5$ nanocomposites can be excited by visible light to produce carriers. When composing g-C_3N_4 and $MgTi_2O_5$ to construct heterojunction, due to the different electric potential, the photogenerated carriers can transfer between the interfaces of two photoconductors. The photoinduced electrons gather in the CB of $MgTi_2O_5$ and holes in the VB of g-C_3N_4, which efficiently reach our objective to suppress the recombination of photogenerated charge carriers. The photogenic electrons transition between g-C_3N_4 and $MgTi_2O_5$ was an important reason for effectively improving the photocatalytic abilities of g-C_3N_4.

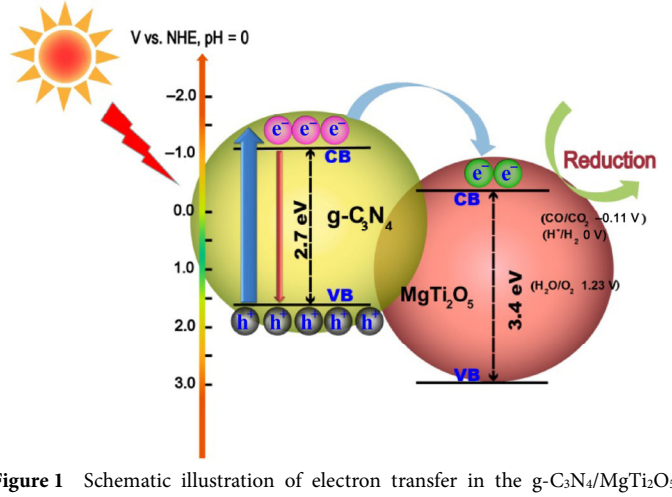

Figure 1 Schematic illustration of electron transfer in the g-C_3N_4/$MgTi_2O_5$ nanocomposites under visible light.

2 Experimental

All chemical reagents are analytic grade and were used as received without further purification. The g-C_3N_4 was immediately obtained by annealing of urea. They were annealed at 600 °C for 2 h in N_2 atmosphere. Briefly, a certain amount of g-C_3N_4 was dispersed into methanol (25 mL) in a beaker, the mixture was sonicated with a sonifier for about 30 min, after that, 5 wt.% $MgTi_2O_5$ powder was then added. The organic solvent was removed by stirring the mixture for 24 h. After drying the products in N_2 atmosphere, the g-C_3N_4/$MgTi_2O_5$ nanocomposite was obtained. Other comparative materials were prepared in the same way. For comparison, the mass percentage of $MgTi_2O_5$ was accounted for 5%, 10%, 15% of the mass of g-C_3N_4, respectively, and denoted as CN-MTO-*X* (*X* = 5, 10 and 15), where X denotes the $MgTi_2O_5$ content in wt.%, respectively.

3 Results and discussion

As shown in Figs. 2(a) and 2(b), the photocatalytic activities of g-C_3N_4/$MgTi_2O_5$ nanocomposites with 5 wt.% and 15 wt.% $MgTi_2O_5$ content were evaluated for photocatalytic H_2 production for 4 h. The H_2 production rate of the g-C_3N_4 was investigated to be 299.3 $\mu mol \cdot g^{-1} \cdot h^{-1}$. When composing with $MgTi_2O_5$, the photocatalytic activity of g-C_3N_4 was dramatically improved. And CN-MTO-5 displayed the highest hydrogen production rate (666.09 $\mu mol \cdot g^{-1} \cdot h^{-1}$), which was about two-fold higher than that of g-C_3N_4 (299.3 $\mu mol \cdot g^{-1} \cdot h^{-1}$), it shows that the photocatalytic activity were improved after compositing g-C_3N_4 with $MgTi_2O_5$. However, when the amount of $MgTi_2O_5$ in g-C_3N_4/$MgTi_2O_5$ nanocomposites rose to 15 wt.%, resulting a lower H_2 evolution rate (562 $\mu mol \cdot g^{-1} \cdot h^{-1}$). Thus, it indicates that CN-MTO-5 is the amount-optimized one to photocatalytic hydrogen production. As shown in Fig. S1 in the Electronic Supplementary Material (ESM), the XRD indicates no significant change before and after hydrogen production, which was attributed to stability of as-prepared samples.

In order to further identify the enhanced photocatalytic performance of the nanocomposites, the CO_2 reduction activities was investigated under visible light for 6 h in Figs. 3(a)–3(c). Obviously, the CO_2 reduction performance of g-C_3N_4 was measured to CO (~ 1.75 $\mu mol \cdot g^{-1} \cdot h^{-1}$), CH_4 (~ 0.5 $\mu mol \cdot g^{-1} \cdot h^{-1}$) and O_2 (~ 10.2 $\mu mol \cdot g^{-1} \cdot h^{-1}$), after decorated with 5 wt.% $MgTi_2O_5$, the photocatalytic performance was largely increased to CO (~ 11.534 $\mu mol \cdot g^{-1} \cdot h^{-1}$), CH_4 (~ 4.28 $\mu mol \cdot g^{-1} \cdot h^{-1}$) and O_2 (~ 24.92 $\mu mol \cdot g^{-1} \cdot h^{-1}$). Furthermore, the $MgTi_2O_5$ is an outstanding platform in terms of the increased activities of g-C_3N_4. To further demonstrate the impact of $MgTi_2O_5$ on the nanocomposites, we measured the CO_2 reduction performance of g-C_3N_4/$MgTi_2O_5$ nanocomposites with different amount of $MgTi_2O_5$ as comparative experiment. As shown in Fig. 3(b), it is clear that the CO production rate of them increases 1.86, 6.59, 5.28, and 4.76 times for 3 wt.%, 5 wt.%, 10 wt.%, 15 wt.% $MgTi_2O_5$ in g-C_3N_4/$MgTi_2O_5$ nanocomposites compared with g-C_3N_4. The CN-MTO-5 shows the highest production rate, which dramatically increased with $MgTi_2O_5$ content to maximum at 5%, and then decreased upon further increasing $MgTi_2O_5$. As shown in Fig. 3(c), the production rate of CO almost unchanged in 5 cyclic experiments which can easily indicate its superior stability. The separation and recombination of photogenic carriers can be measured access to surface photo-voltage spectra (SPS), it is an effective method to detect the photogenerated electron separation. Generally, the stronger SPS signal and the higher photogenic electrons separation can be illustrated. It was illustrated that g-C_3N_4 and $MgTi_2O_5$ show a low SPS response (Fig. 3(d)). However, the SPS response signal of

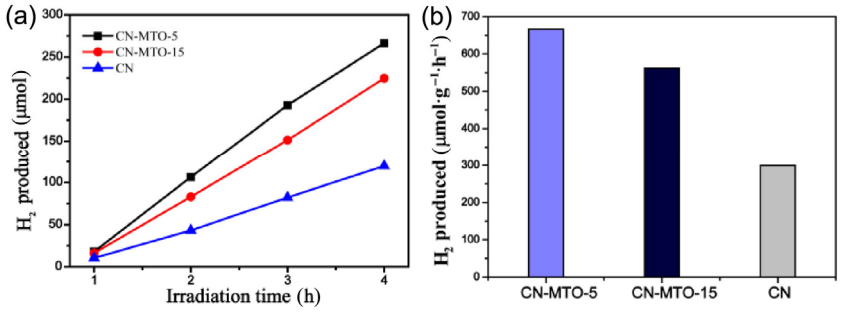

Figure 2 (a) and (b) Photocatalytic hydrogen production rates for the CN (g-C_3N_4), CN-MTO-5 and CN-MTO-15.

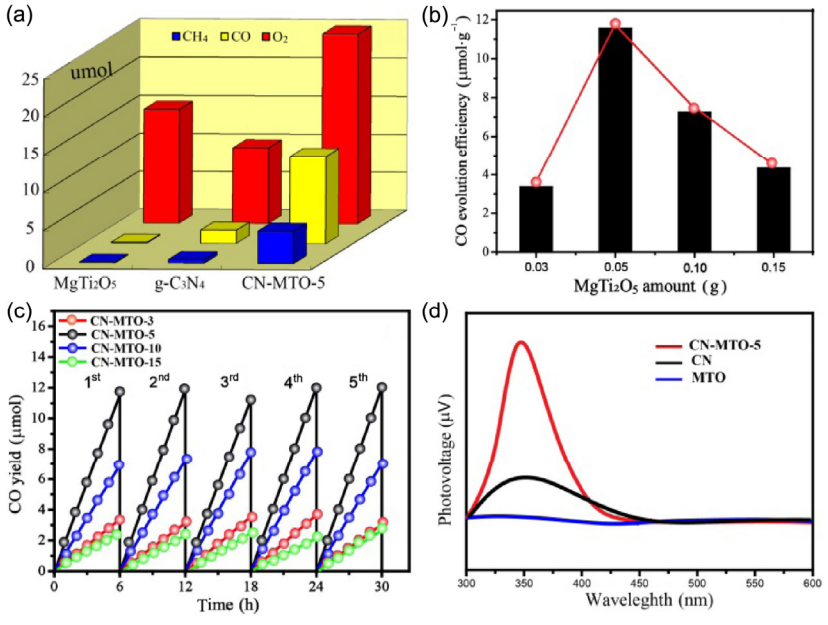

Figure 3 (a) Photocatalytic CO_2 reduction for MTO, CN, CN-MTO-5 samples under visible light irradiation. (b) CO evolution amount of MTO (column chart) within 6 h with the amount of MTO (0.03, 0.05, 0.10, and 0.15 g) and 1 g of g-C_3N_4 nanosheets under visible light irradiation. (c) Cyclic photocatalysis CO_2 reduction curves. (d) Surface photo-voltage spectra of CN (g-C_3N_4), MTO ($MgTi_2O_5$) and CN-MTO-5.

CN-MTO-5 was the highest compared with g-C_3N_4 and $MgTi_2O_5$. It illustrates the separation efficiency of photogenic carriers has been obviously enhanced, which can further verify the excellent performance of the nanocomposites. At the same time, the CN-MTO-5 also has high performance under solar light. As shown in Fig. S2 in the ESM, the CO production rate of CN-MTO-5 is 31.25 $\mu mol \cdot g^{-1} \cdot h^{-1}$, and the yield of CH_4 is 4.38 $\mu mol \cdot g^{-1} \cdot h^{-1}$.

As shown in Fig. 4(a), the photo-current curves of the CN-MTO-5 nanocomposites exhibit highest response signal under visible light, during the five turn on-off cycles, which demonstrate the enhanced photo-induced carriers' separation efficiency. At the same time, in order to deeper evaluate the electron transfer in a dark phenomenon, the electrochemical impedance spectroscopy (EIS) was investigated in a light deficient situation. It can easily conclude that the interfacial impedance of CN-MTO-5 exhibits the smallest semicircle curves compared with other as-prepared products, which can also indicate the lowest charge resistance. It can identify-twice the separation efficiency of charge has extremely improved. Therefore, we can reach a conclusion that the CN-MTO-5 was the optimal proportion of nanocomposites to boost the charge transport. As illustrated in Fig. S8 in the ESM, the positive slopes of Mott-Schottky plot displays n-type semiconductor characteristics for g-C_3N_4 and CN-MTO-5, it is worth noting that the higher slope of the plot, the lower electronic charge intensive can be measured, which can conclude that the CN-MTO-5 has the much higher charge intensity than g-C_3N_4. The electrochemical CO_2 reduction experiments of g-C_3N_4, CN-MTO-5, CN-MTO-10, and CN-MTO-15 were measured. As shown in Fig. 4(c), then the possible reason of the improved photocatalytic CO_2 reduction performance can be evaluated. The current response of CN-MTO-5 is still the optimum, and the superior performance of the nanocomposites has been further proved. The photoluminescence (PL) was used to verify the efficiency of the electrons transitions between the interfaces of two semiconductors. The emission density of g-C_3N_4 decreases with coupling a verity amount of $MgTi_2O_5$, and the CN-MTO-5 exhibits the weak PL signal, since the photoluminescence intensity related to the recombination of charge carriers, and the quenching of fluorescence can be revealed by increasing the amount of $MgTi_2O_5$ to some extent, demonstrating that the positive role of $MgTi_2O_5$ in enhancing the separation efficiency of electrons and holes. Thus, CN-MTO-5 has lower interface resistance and higher electronic charge density, stronger photocurrent intensity and superior photocatalytic CO_2 reduction performance. These results give bright evidence that CN-MTO-5 can extremely facilitate the separation of photogenic carriers.

To confirm the synthetic product composition, the X-ray diffraction (XRD) patterns were evaluated. Figure 5(a) shows the XRD pattern of hexagonal phase g-C_3N_4. The pure g-C_3N_4 catalyst exhibits an obvious peak at 27.3°, which were indexed as (002) diffraction plane (JCPDS 87-1526). And the diffraction peaks of as-prepared in accordance with the peak of pure orthorhombic phase $MgTi_2O_5$ (JCPDS 35-0792). No other impurity peaks such as TiO_2, $MgTiO_3$ and Mg_2TiO_4 were detected. The results indicated that $MgTi_2O_5$ and g-C_3N_4 coexist in g-C_3N_4/$MgTi_2O_5$ nanocomposites, and the crystal phase of two materials in g-C_3N_4/$MgTi_2O_5$ keeps unchanged after

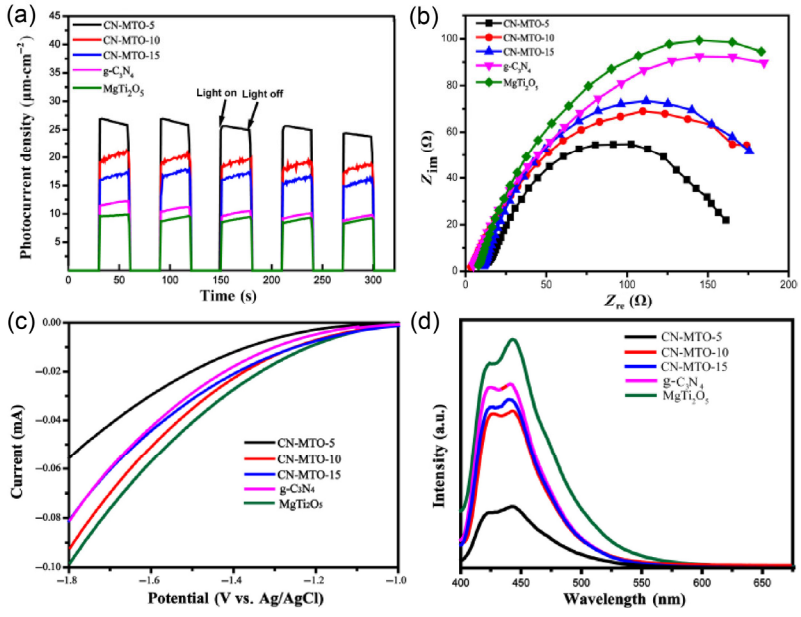

Figure 4 (a) Transient photocurrent responses. (b) Nyquist plots of electrochemical impedance. (c) Electrochemical CO_2 reduction, and (d) PL spectra.

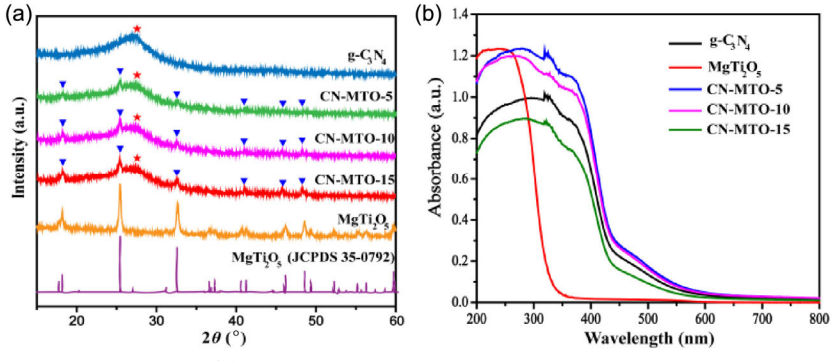

Figure 5 (a) XRD patterns and (b) UV–vis DRS spectra of the as-prepared g-C_3N_4, $MgTi_2O_5$, CN-MTO-5, CN-MTO-10, and CN-MTO-15.

constructing nanocomposites. The absorption change can be measured by UV–Vis DRS. As shown in Fig. 5(b) spectra, both g-C_3N_4 and as-prepared g-C_3N_4/$MgTi_2O_5$ nanocomposites indicate the visible-light absorption. Compared with g-C_3N_4 and nanocomposites UV–Vis DRS, the CN-MTO-5 shows the higher absorption intensity, it may give evidences to its superior photocatalytic performance. In addition, the DRS spectrum of g-C_3N_4/$MgTi_2O_5$ composites exhibits absorption amplification at 300 nm, demonstrating the successfully built a g-C_3N_4/$MgTi_2O_5$ nanocomposites. The specific surface area is measured from N_2 adsorption–desorption isotherms. As shown in Fig. S3 in the ESM, it is clear that the consequence of BETs has no obvious change, which exhibits the surface area is not major factor for its superior performance.

The TEM and SEM images show the morphology and structure of as-prepared products. It is measured that the SEM and TEM images of as-prepared g-C_3N_4/$MgTi_2O_5$ nanocomposites were nearly consistent with the XRD results. Based on the SEM and TEM images of g-C_3N_4 and CN-MTO-5 in Figs. 6(a)–6(d), it is clear that the $MgTi_2O_5$ nanorods are composited with g-C_3N_4 successfully in Fig. 6(d). In addition, the HRTEM image in Fig. 6(e), $MgTi_2O_5$ and g-C_3N_4 have exhibited a close combination. The clear lattice fringes can be observed in images, and the distance of the inter-planar was measured about 0.27 nm, which was indexed to $MgTi_2O_5$. In summary, the nanocomposites consisted of g-C_3N_4 and $MgTi_2O_5$ have been successfully constructed. And the close combination of g-C_3N_4 and $MgTi_2O_5$ can play a positive role in facilitating the transition of electronic charge in the heterojunction nanocomposites.

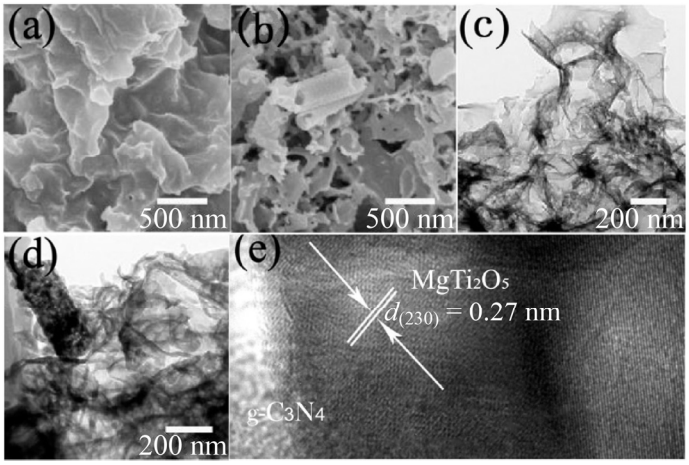

Figure 6 (a) and (b) SEM images of g-C_3N_4 and CN-MTO-5. (c) and (d) TEM images of g-C_3N_4 and CN-MTO-5. (e) HRTEM images of CN-MTO-5.

To better verify the elemental chemical states, the XPS survey spectra were investigated. As indicated in Fig. 7(a), the presence of Mg, C, N, Ti, and O elements was obviously exhibited in CN-MTO-5. In Fig. 7(b), the strong peak of Mg 2p at 49.7 eV is ascribed to Mg $2p_{3/2}$, and it is characteristic of Mg^{2+} in $MgTi_2O_5$. In Fig. 7(c), two distinct peaks located at 458.6 and 464.1 eV are ascribed to Ti $2p_{3/2}$ and Ti $2p_{1/2}$, which are typical for the Ti^{4+} species in $MgTi_2O_5$. In Fig. 7(d), the XPS spectrum of O 1s was fitted into three contributions

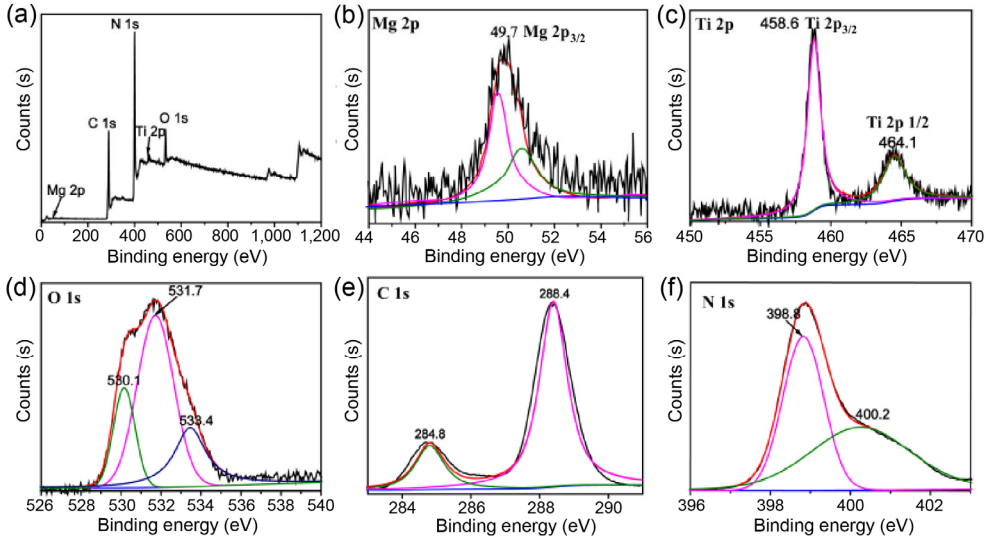

Figure 7 XPS fully scanned spectrum of sample CN-MTO-5 (a). (b)–(f) High-resolution XPS spectra for Mg 2p, Ti 2p, O 1s, C 1s, and N 1s.

resulting from Gaussian rule. These peaks located at 530.1, 531.7, and 533.4 eV, which can be assigned to lattice oxygen, adsorbed oxygen, and hydroxyl oxygen, respectively. It is clear that binding energy value of O 1s is moved to higher energy side after compositing $MgTi_2O_5$ in Fig. S5 in the ESM. In Fig. 7(e), it is obvious that the peaks of the C 1s are located at 284.6 and 288.4 eV. The peak at 284.6 eV can be assigned to C–C. Another peak located at 288.4 eV is the characteristic peak of N–C–N was related to g-C_3N_4. In Fig. 7(f) the obvious peaks of N 1s on CN-MTO-5 are attributed at 398.8 and 400.2 eV, respectively. The major peak was located at 398.8 eV attributed to sp^2 hybridized nitrogen (C=N–C), which exhibits the appealing of sp^2 bonded carbon nitride and another peak at 400.2 eV can be attributed to N-$(C)^3$ groups. It is noticed from Fig. S7 in the ESM and Figs. 7(e) and 7(f), that the N 1s and C 1s (C=N) moved into the lower energy side after constructing the nanocomposites, demonstrating the electron delocalization effect. Thus, it is deduced that the $MgTi_2O_5$ is successfully incorporated into the g-C_3N_4/$MgTi_2O_5$ nanocomposites, which would benefit for charge transfer and the peak position of each element of CN-MTO-5 nanocomposites and the valence state of each element have basically no change, the valence states of Mg and Ti are +2 and +4.

The X-ray energy dispersive spectroscopy (EDS) showed in Fig. S9 in the ESM that the elemental composition of the g-C_3N_4, pure $MgTi_2O_5$ and CN-MTO-5 can be characterized. In Fig. S9(a) in the ESM, it detected two elements, C and N, combined with other results which can illustrate the g-C_3N_4 was obtained. In Fig. S9(b) in the ESM, the results illustrated that the Mg, Ti, and O was detected in the $MgTi_2O_5$ patterns. The atomic ratio of Ti and Mg was about 1:1, which demonstrated the $MgTi_2O_5$ was successfully prepared. Successful synthesis of target products can be demonstrated by XRD and XPS. The EDS spectra analyses in Fig. S9(c) can also support the results, as only Mg, Ti, O, C and N can be probed.

4 Conclusion

In conclusion, we designed a photocatalyst with the superior photocatalytic performance, which was prepared via a facial method for composing $MgTi_2O_5$ with g-C_3N_4 to construct nanocomposites. And the photocatalytic performance for H_2 production and CO_2 conversion of CN-MTO nanocomposites under visible light were systematically studied. The CN-MTO-5, the amount-optimized one, exhibits the superior photocatalytic performance with the H_2 production rate of 666.09 $\mu mol \cdot g^{-1} \cdot h^{-1}$, and also exists superior CO_2 reduction performance of the yield of CO (11.534 $\mu mol \cdot g^{-1} \cdot h^{-1}$), CH_4 (4.28 $\mu mol \cdot g^{-1} \cdot h^{-1}$) and O_2 (24.92 $\mu mol \cdot g^{-1} \cdot h^{-1}$) under visible irradiation. These excellent performances result from the reasonable structure of CN-MTO nanocomposites, which can efficiently enhance the separation efficiency of the electron-hole pairs, and largely extend the lifetime, and extremely decrease the energy loss. It successfully improved the photocatalytic performance of g-C_3N_4, and overcame its shortcomings by introducing $MgTi_2O_5$ as a reasonable platform to improve the photocatalytic activities for g-C_3N_4.

Acknowledgements

This work was supported by the National Natural Science Foundation of China (Nos. 21871079 and 21501052).

Electronic Supplementary Material: Supplementary material (characterization of UCNPs with TEM, XRD, and absorption spectroscopy, time resolved data, calculation of the triphotonic population contribution of the red emission band, description of fitting procedure, results of rate equation analysis) is available in the online version of this article at https://doi.org/10.1007/s12274-019-2460-2.

References

[1] Fujishima, A.; Honda, K. Electrochemical photolysis of water at a semiconductor electrode. *Nature* **1972**, *238*, 37–38.

[2] Muhammad, N. A.; Wang, Y. J.; Muhammad, F. E.; He, T. Photoreduction of carbon dioxide using strontium zirconate nanoparticles. *Sci. China Mater*. **2015**, *58*, 634–639.

[3] Meng, X. G.; Zuo, G. F.; Zong, P. X.; Pang, H.; Ren, J.; Zeng, X. F.; Liu, S. S.; Shen, Y.; Zhou, W.; Ye, J. H. A rapidly room-temperature-synthesized Cd/ZnS:Cu nanocrystal photocatalyst for highly efficient solar-light-powered CO_2 reduction. *Appl. Catal. B: Environ*. **2018**, *237*, 68–73.

[4] Lei, Y. P.; Shi, Q.; Han, C.; Wang, B.; Wu, N.; Wang, H.; Wang, Y. D. N-doped graphene grown on silk cocoon-derived interconnected carbon fibers for oxygen reduction reaction and photocatalytic hydrogen production. *Nano Res*. **2016**, *9*, 2498–2509.

[5] Habisreutinger, S. N.; Schmidt-Mende, L.; Stolarczyk, J. K. Photocatalytic reduction of CO_2 on TiO_2 and other semiconductors. *Angew. Chem., Int. Ed*. **2013**, *52*, 7372–7408.

[6] Shan, J. J.; Raziq, F.; Humayun, M.; Zhou, W.; Qu, Y.; Wang, G. F.; Li, Y. D. Improved charge separation and surface activation via boron-doped layered polyhedron $SrTiO_3$ for co-catalyst free photocatalytic CO_2 conversion. *Appl. Catal. B: Environ*. **2017**, *219*, 10–17.

[7] Jang, Y. J.; Jang, J. W.; Lee, J.; Kim, J. H.; Kumagai, H.; Lee, J.; Minegishi, T.; Kubota, J.; Domen, K.; Lee, J. S. Selective CO production by Au coupled ZnTe/ZnO in the photoelectrochemical CO_2 reduction system. *Energy*

Environ. *Sci*. **2015**, *8*, 3597–3604.
[8] Zhang, N.; Qu, Y.; Pan, K.; Wang, G. F.; Li, Y. D. Synthesis of pure phase $Mg_{1.2}Ti_{1.8}O_5$ and $MgTiO_3$ nanocrystals for photocatalytic hydrogen production. *Nano Res*. **2016**, *9*, 726–734.
[9] Wang, D. S.; Xie, T.; Li, Y. D. Nanocrystals: Solution-based synthesis and applications as nanocatalysts. *Nano Res*. **2009**, *2*, 30–46.
[10] Zhu, M. S.; Chen, P. L.; Liu, M. H. Visible-light-driven Ag/Ag_3PO_4-based plasmonic photocatalysts: Enhanced photocatalytic performance by hybridization with graphene oxide. *Chin*. *Sci*. *Bull*. **2013**, *58*, 84–91.
[11] Wang, H. T.; Wu, X.; Zhao, H. M.; Quan, X. Enhanced photocatalytic degradation of tetracycline hydrochloride by molecular imprinted film modified TiO_2 nanotubes. *Chin*. *Sci*. *Bull*. **2012**, *57*, 601–605.
[12] Zhang, X. D.; Wang, H. X.; Wang, H.; Zhang, Q.; Xie, J. F.; Tian, Y. P.; Wang, J.; Xie, Y. Single-layered graphitic-C_3N_4 quantum dots for two-photon fluorescence imaging of cellular nucleus. *Adv*. *Mater*. **2014**, *26*, 4438–4443.
[13] Chen, D. D.; Wu, I. C.; Liu, Z. H.; Tang, Y.; Chen, H. B.; Yu, J. B.; Wu, C. F.; Chiu, D. T. Semiconducting polymer dots with bright narrow-band emission at 800 nm for biological applications. *Chem*. *Sci*. **2017**, *8*, 3390–3398.
[14] Sun, K.; Yang, Y. K.; Zhou, H.; Yin, S. Y.; Qin, W. P.; Yu, J. B.; Chiu, D. T.; Yuan, Z.; Zhang, X. J.; Wu, C. F. Ultrabright polymer-dot transducer enabled wireless glucose monitoring via a smartphone. *ACS Nano* **2018**, *12*, 5176–5184.
[15] Tang, S. F.; Yin, X. P.; Wang, G. Y.; Lu, X. L.; Lu, T. B. Single titanium-oxide species implanted in 2D g-C_3N_4 matrix as a highly efficient visible-light CO_2 reduction photocatalyst. *Nano Res*. **2019**, *12*, 457–462.
[16] Peng, W. C.; Li, X. Y. Synthesis of a sulfur-graphene composite as an enhanced metal-free photocatalyst. *Nano Res*. **2013**, *6*, 286–292.
[17] Xiao, M.; Luo, B.; Wang, S. C.; Wang, L. Z. Solar energy conversion on g-C_3N_4 photocatalyst: Light harvesting, charge separation, and surface kinetics. *J*. *Energy Chem*. **2018**, *27*, 1111–1123.
[18] Fu, J. W.; Yu, J. G.; Jiang, C. J.; Cheng, B. g-C_3N_4-based heterostructured photocatalysts. *Adv*. *Energy Mater*. **2018**, *8*, 1701503.
[19] Wang, Y. Y.; Bai, L. L.; Zhang, Z. Q.; Qu, Y.; Jing, L. Q. Improved visible-light photoactivity of Pt/g-C_3N_4 nanosheets for solar fuel production via pretreated boric acid modification. *Res*. *Chem*. *Intermed*. **2019**, *45*, 249–259.
[20] Wang, X. C.; Maeda, K.; Thomas, A.; Takanabe, K.; Xin, G.; Carlsson, J. M.; Domen, K.; Antonietti, M. A metal-free polymeric photocatalyst for hydrogen production from water under visible light. *Nat*. *Mater*. **2009**, *8*, 76–80.
[21] Liu, W.; Cao, L. L.; Cheng, W. R.; Cao, Y. J.; Liu, X. K.; Zhang, W.; Mou, X. L.; Jin, L. L.; Zheng, X. S.; Che, W. et al. Single-site active cobalt-based photocatalyst with a long carrier lifetime for spontaneous overall water splitting. *Angew*. *Chem*., *Int*. *Ed*. **2017**, *56*, 9312–9317.
[22] Zhang, P.; Ochi, T.; Fujitsuka, M.; Kobori, Y.; Majima, T.; Tachikawa, T. Topotactic epitaxy of $SrTiO_3$ mesocrystal superstructures with anisotropic construction for efficient overall water splitting. *Angew*. *Chem*., *Int*. *Ed*. **2017**, *56*, 5299–5303.
[23] Wan, J. W.; Chen, W. X.; Jia, C. Y.; Zheng, L. R.; Dong, J. C.; Zheng, X. S.; Wang, Y.; Yan, W. S.; Chen, C.; Peng, Q. et al. Defect effects on TiO_2 nanosheets: Stabilizing single atomic site Au and promoting catalytic properties. *Adv*. *Mater*. **2018**, *30*, 1705369.
[24] Waqas, M.; Wei, Y. Z.; Mao, D.; Qi, J.; Yang, Y.; Wang, B.; Wang, D. Multi-shelled TiO_2/Fe_2TiO_5 heterostructured hollow microspheres for enhanced solar water oxidation. *Nano Res*. **2017**, *10*, 3920–3928.
[25] Han, C.; Wang, Y. D.; Lei, Y. P.; Wang, B.; Wu, N.; Shi, Q.; Li, Q. *In situ* synthesis of graphitic-C_3N_4 nanosheet hybridized N-doped TiO_2 nanofibers for efficient photocatalytic H_2 production and degradation. *Nano Res*. **2015**, *8*, 1199–1209.
[26] Herlihy, D. M.; Waegele, M. M.; Chen, X. H.; Pemmaraju, C. D.; Prendergast, D.; Cuk, T. Detecting the oxyl radical of photocatalytic water oxidation at an n-$SrTiO_3$/aqueous interface through its subsurface vibration. *Nat*. *Chem*. **2016**, *8*, 549–555.
[27] Han, C.; Lei, Y. P.; Wang, B.; Wu, C. Z.; Zhang, X. S.; Shen, S. J.; Sun, L.; Tian, Q.; Feng, Q. G.; Wang, Y. D. The functionality of surface hydroxyls on selective CH_4 generation from photoreduction of CO_2 over SiC nanosheets. *Chem*. *Commun*. **2019**, *55*, 1572–1575.
[28] Wang, B.; Wang, Y. D.; Lei, Y. P.; Wu, N.; Gou, Y. Z.; Han, C.; Xie, S.; Fang, D. Mesoporous silicon carbide nanofibers with *in situ* embedded carbon for co-catalyst free photocatalytic hydrogen production. *Nano Res*. **2016**, *9*, 886–898.
[29] Qu, Y.; Zhou, W.; Xie, Y.; Jiang, L.; Wang, J. Q.; Tian, G. H.; Ren, Z. Y.; Tian, C. H.; Fu, H. G. A novel phase-mixed $MgTiO_3$-$MgTi_2O_5$ heterogeneous nanorod for high efficiency photocatalytic hydrogen production. *Chem*. *Commun*. **2013**, *49*, 8510–8512.
[30] Wu, N. Q.; Wang, J.; Tafen, D. N.; Wang, H.; Zheng, J. G.; Lewis, J. P.; Liu, X. G.; Leonard, S. S.; Manivannan, A. Shape-enhanced photocatalytic activity of single-crystalline anatase TiO_2 (101) nanobelts. *J*. *Am*. *Chem*. *Soc*. **2010**, *132*, 6679–6685.
[31] Cui, Q. Z.; Dong, X. T.; Wang, J. X.; Li, M. Direct fabrication of cerium oxide hollow nanofibers by electrospinning. *J*. *Rare Earths* **2008**, *26*, 664–669.
[32] Cheng, L.; Liu, P.; Qu, S. X.; Cheng, L.; Zhang, H. W. Microwave dielectric properties of Mg_2TiO_4 ceramics synthesized via high energy ball milling method. *J*. *Alloys Compd*. **2015**, *623*, 238–242.
[33] Ullah, U.; Ali, W. F. F. W.; Ain, M. F.; Mahyuddin, N. M.; Ahmad, Z. A. Design of a novel dielectric resonator antenna using $MgTiO_3$–$CoTiO_3$ for wideband applications. *Mater*. *Des*. **2015**, *85*, 396–403.
[34] Zhao, B.; Liu, Z. R.; Liu, Z. L.; Liu, G. X.; Li, Z.; Wang, J. X.; Dong, X. T. Silver microspheres for application as hydrogen peroxide sensor. *Electrochem*. *Commun*. **2009**, *11*, 1707–1710.
[35] Ma, Y. X.; Li, H.; Peng, S.; Wang, L. Y. Highly selective and sensitive fluorescent paper sensor for nitroaromatic explosive detection. *Anal*. *Chem*. **2012**, *84*, 8415–8421.
[36] Meng, L.; Ren, Z. Y.; Zhou, W.; Qu, Y.; Wang, G. F. $MgTiO_3/MgTi_2O_5/TiO_2$ heterogeneous belt-junctions with high photocatalytic hydrogen production activity. *Nano Res*. **2017**, *10*, 295–304.
[37] Zhang, N.; Zhang, K. F.; Zhou, W.; Jiang, B. J.; Pan, K.; Qu, Y.; Wang, G. F. Pure phase orthorhombic $MgTi_2O_5$ photocatalyst for H_2 production. *RSC Adv*. **2015**, *5*, 106151–106155.
[38] Mortazavi-Derazkola, S.; Salavati-Niasari, M.; Amiri, O.; Abbasi, A. Fabrication and characterization of Fe_3O_4@SiO_2@TiO_2@Ho nanostructures as a novel and highly efficient photocatalyst for degradation of organic pollution. *J*. *Energy Chem*. **2017**, *26*, 17–23.